Article

Structural basis of peptide recognition and activation of endothelin receptors

Yujie Ji[1,2,8], Jia Duan[1,2,3,8] ✉, Qingning Yuan[1,8], Xinheng He [1,2], Gong Yang[4], Shengnan Zhu[5], Kai Wu[1], Wen Hu[1], Tianyu Gao[6], Xi Cheng [1,2], Hualiang Jiang [1,2,6,7], H. Eric Xu [1,2,6] ✉ & Yi Jiang [6,7] ✉

Endothelin system comprises three endogenous 21-amino-acid peptide ligands endothelin-1, -2, and -3 (ET-1/2/3), and two G protein-coupled receptor (GPCR) subtypes−endothelin receptor A (ET$_A$R) and B (ET$_B$R). Since ET-1, the first endothelin, was identified in 1988 as one of the most potent endothelial cell-derived vasoconstrictor peptides with long-lasting actions, the endothelin system has attracted extensive attention due to its critical role in vasoregulation and close relevance in cardiovascular-related diseases. Here we present three cryo-electron microscopy structures of ET$_A$R and ET$_B$R bound to ET-1 and ET$_B$R bound to the selective peptide IRL1620. These structures reveal a highly conserved recognition mode of ET-1 and characterize the ligand selectivity by ETRs. They also present several conformation features of the active ETRs, thus revealing a specific activation mechanism. Together, these findings deepen our understanding of endothelin system regulation and offer an opportunity to design selective drugs targeting specific ETR subtypes.

Endothelin receptors (ETRs) are comprised of two subtypes (ET$_A$R[1] and ET$_B$R[2]) with ~60% sequence similarity, both of which belong to the class A G protein-coupled receptors (GPCRs)[3]. ETRs are widely expressed in the human body, with ET$_A$R primarily expressed in the cardiovascular system[4] and ET$_B$R in the brain[5]. They are activated by three types of endothelin (ET-1, ET-2, and ET-3), 21-amino-acid peptide hormones[6,7]. Besides, naturally occurring sarafotoxins (s6a–d), isolated from snake venom, show a high degree of sequence similarity and biological effects with ET-1 (Fig. 1a)[8]. Both ET$_A$R and ET$_B$R show different responses to these peptide agonists. ET$_A$R exhibits similar sub-nanomolar affinities to ET-1 and ET-2 but a 100-fold weaker affinity to ET-3, while three ETs are equally effective for ET$_B$R[9,10]. Sarafotoxin s6c shows a 100- to 10,000-fold reduced affinity for ET$_A$R compared with s6b, thus producing a substantial ET$_B$R selectivity[11]. Upon binding by agonists, ET$_A$R primarily couples to the G$_q$ protein, while ET$_B$R couples to multiple G proteins, including G$_s$, G$_i$, and G$_q$ proteins, to transduce signals (Fig. 1b, data from GPCRdb.org[12]). Intriguingly, two ETR

subtypes exert opposing actions on vasoregulation: ET-1-mediated ET$_A$R activation promotes long-lasting vasoconstriction, while ET$_B$R mediates vasodilation and can inhibit the ET-1-mediated effects upon activated by ET-3, thus being considered a physiological antagonist of ET$_A$R[13,14].

The endothelin system has ignited extensive interest in its utmost importance in cardiovascular system regulation. Dysregulation of the endothelin system, especially the ET$_A$R receptor, is closely associated with arterial hypertension, atherosclerosis, heart failure, renal disease, diabetes, etc., making ETRs promising drug targets for the treatment of these diseases[9,10,14]. Several non-selective ETRs antagonists (bosentan and macitentan) and ET$_A$R-selective antagonists (ambrisentan and clazosentan) have been approved for the treatment of pulmonary arterial hypertension (PAH). ET$_B$R-selective agonist Succinyl-[Glu[9], Ala[11,15]]-ET-1(8-21), also named IRL1620[15], is also in clinical trials for adjuvant cancer therapy to enhance the delivery of anti-tumor drugs by improving blood flow[16]. Thus, developing selective ligands

[1]State Key Laboratory of Drug Research, Shanghai Institute of Materia Medica, Chinese Academy of Sciences, Shanghai 201203, China. [2]University of Chinese Academy of Sciences, Beijing 100049, China. [3]Zhongshan Institute for Drug Discovery, Zhongshan, China. [4]State Key Laboratory of Cellular Stress Biology, School of Life Sciences, Xiamen University, Fujian 361005, China. [5]School of Pharmacy, Macau University of Science and Technology, Macau 999078, China. [6]School of Life Science and Technology, ShanghaiTech University, Shanghai 201210, China. [7]Lingang Laboratory, Shanghai 200031, China. [8]These authors contributed equally: Yujie Ji, Jia Duan, Qingning Yuan. ✉e-mail: duanjia@simm.ac.cn; eric.xu@simm.ac.cn; yjiang@lglab.ac.cn
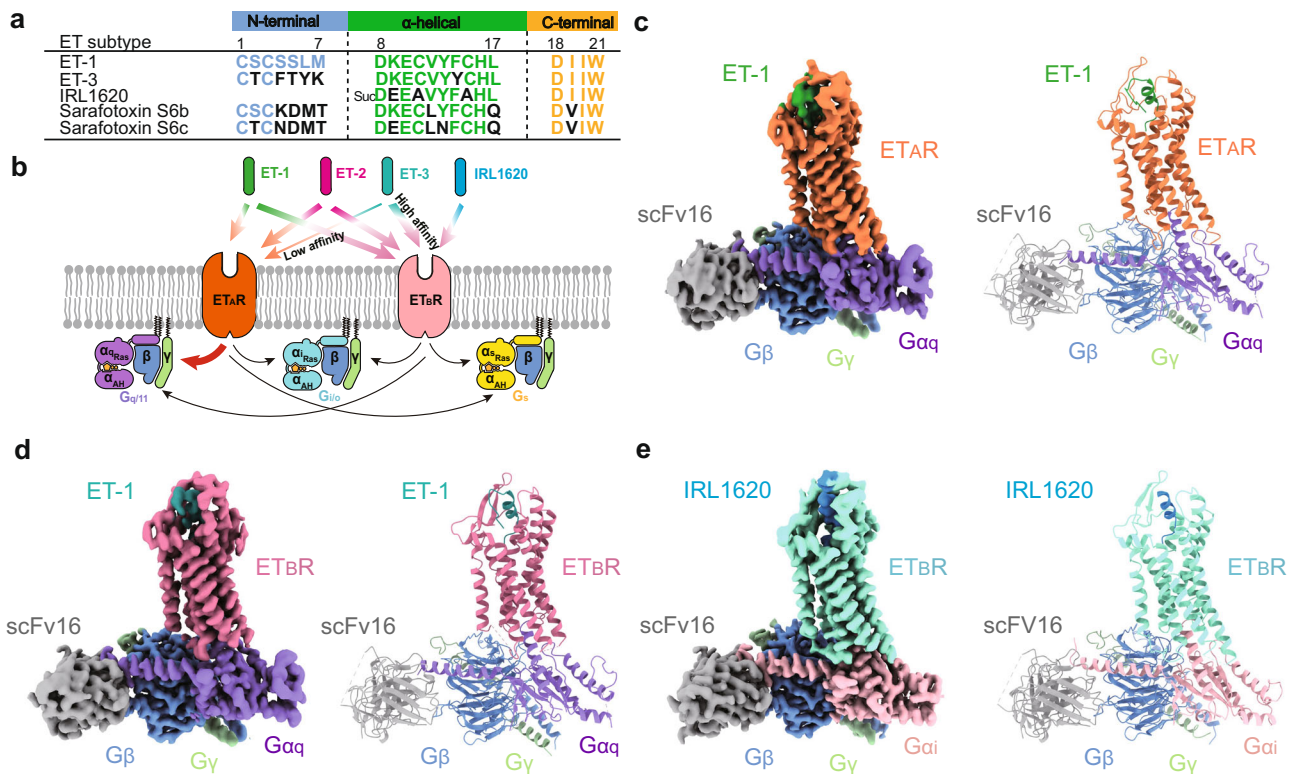
Fig. 1 | Cryo-EM structures of ET-1-ET$_A$R-G$_q$, ET-1-ET$_B$R-G$_q$, and IRL1620-ET$_B$R-G$_i$ complexes. a Sequence comparison of peptides, including ET-1, ET-3, IRL1620, sarafotoxin S6b, and S6c. The N-terminal, α-helical, and C-terminal regions of peptides are colored blue, green, and yellow, respectively. Residues different from that of ET-1 are colored black. **b** Schematic illustration of G protein-coupling of ETRs activated by endothelin and IRL1620. **c–e** Cryo-EM density maps (left panel) and cartoon representation (right panel) of ET-1-ET$_A$R-G$_q$-scFv16 (**c**), ET-1-ET$_B$R-G$_q$-scFv16 (**d**), and IRL1620-ET$_B$R-G$_i$-scFv16 complexes (**e**). Components of ETRs complexes are colored as indicated.

targeting specific endothelin receptor subtypes is of great pharmacology interest.

Extensive efforts have been made to clarify the recognition and activation mechanism of ETRs. Structural and relationship analysis had clarified residues on ET-1 crucial for binding[17–19]. Crystal structures of ET$_B$R bound to endogenous peptides, including ET-1, ET-3, s6b, and synthesized agonists or antagonists were subsequently released, thus offering molecular evidence on ET$_B$R recognition by ligands and receptor activity regulation[11,20–23]. In addition, different architectures of ECL2 of ET$_A$R and ET$_B$R were suggested to account for the selectivity of ET isopeptides[22]. A structure-based molecular simulation revealed that E9 in sarafotoxin s6c may rearrange its interaction with extracellular regions, subsequently destabilize its interaction with ET$_A$R, thus leading to reduced ET$_A$R affinity and ET$_B$R specificity[11]. However, the inaccessible structural information on the ET$_A$R subtype hampers our understanding of mechanisms of ligand recognition by ET$_A$R, ligand selectivity, and ET$_A$R activation. In this study, we present cryo-electron microscopy (cryo-EM) structures of engineered G protein-coupled ET$_A$R and ET$_B$R bound to ET-1 and ET$_B$R bound to the selective peptide IRL1620. These structures reveal the molecular mechanism of peptide agonists recognition by ET$_A$R and characterize the ligand selectivity and activation features for ETRs.

Results

Structure determination of ET$_A$R and ET$_B$R complexes

The NanoBiT tethering strategy, which has been used to stabilize the GPCR-G protein complex[24], was introduced to facilitate the assembly of three endothelin receptor complexes. The large subunit (LgBiT, 18 kDa) and a complimentary peptide (HiBiT, VSGWRLFKKIS) with high affinity for LgBiT were fused to C-termini of the receptor and the Gβ

subunit, respectively (Supplementary Fig. 1). The complementation of LgBiT and HiBiT facilitates the stabilization of ETR and G protein. The chimeric mini-Gα$_q$ used for the assembly of ETR complexes is the GTPase domain of the Gα$_q$ subunit with its N-terminal 35 amino acids replaced by the corresponding sequence in Gα$_{i2}$ to facilitate binding of a single-chain variable fragment (scFv16). It has been successfully applied in the structural determination of the 5-HT$_{2A}$-Gα$_q$ complex[25]. The Gα$_i$ subunit was engineered by introducing two dominant-negative mutations, G203A and A326S, to increase the stability of the ET$_B$R-G$_i$ protein complex[26]. Unless otherwise specified, G$_q$ and G$_i$ refer to respective engineered G proteins, which are used in the structural studies of ETR complexes. The structure of ET-1 bound ET$_A$R and ET$_B$R in complex with engineered G$_q$ heterotrimer were determined by single-particle cryo-EM at global resolutions of 3.0 and 3.5 Å. The cryo-EM structure of the engineered G$_i$-coupled ET$_B$R bound to the selective peptide IRL1620 was solved at a resolution of 3.0 Å (Fig. 1c–e, Supplementary Fig. 2, and Supplementary Table 1). The high-quality map allowed accurate model building for receptor residues N66^{NTD} to N378$^{8.52}$, I85^{NTD} to F397$^{8.54}$, and T84^{NTD} to L401$^{8.58}$ (superscripts refer to Ballesteros–Weinstein numbering[27]) for the ET-1-ET$_A$R-G$_q$, ET-1-ET$_B$R-G$_q$, and IRL1620-ET$_B$R-G$_i$ complexes, respectively, which can provide detailed atomic information of the ligand-binding pocket and the receptor-G protein-coupling interface (Fig. 1c–e and Supplementary Fig. 3a–c).

Globally, ET$_A$R and ET$_B$R adopt the canonical seven-transmembrane fold and G protein recruitment manner. All three complexes show a similar overall arrangement, with a root mean square deviation (RMSD) value for Cα atoms of 0.7–1.0 Å (Fig. 2a). At the receptor extracellular portion, both ETRs exhibit a large-scale outward kink at their extracellular end of TM5, which is distinguished

by other class A peptide GPCRs. The kink is stabilized by a polar interaction network comprised of $K^{3.33}$, $E^{4.60}$, $K^{5.38}$, $Y^{5.34}$, and W21 of ET-1 and creates a wide-open pocket to accommodate peptide agonists (Fig. 2b, c). In addition, besides the conserved TM3-ECL2 disulfide bond, ETRs have an additional disulfide bond between C69/C90[NTD] and C341/C358[7.25] for ET_AR/ET_BR. The featured disulfide bond links the receptor N-terminus and the extracellular end of TM7, thus capping the peptide-binding pocket. The compact extracellular interaction may prevent the agonist dissociation and explain the long-lasting activation of ET-1 (Fig. 2d).

Recognition mechanism of ET-1 by ET_AR

The ET-1 comprises the N-terminal (residues C1-M7), α-helical (D8-L17), and C-terminal regions (D18-W21) (Fig. 3a). It adopts a bicyclic architecture, formed by two pairs of intramolecular disulfide bonds (C1–C15 and C3–C11) (Fig. 3b), as observed in crystal and nuclear magnetic resonance (NMR) structures[18,28]. A previous NMR study identified a stable conformation of the N-terminal and α-helical regions in solution, whereas the C-terminal region is flexible[28]. The C-terminal region of ETs fixes its conformation by inserting it into the receptor core. The extreme C-terminal amino acid W21 makes an H-bond with $K166^{3.33}$ and faces hydrophobic residues $V169^{3.36}$, $L259^{5.42}$, $W319^{6.48}$, $L322^{6.51}$, and $I355^{7.39}$. Its backbone CO also forms an H-bond with $K166^{3.33}$. I19 and I20 are buried in a hydrophobic cavity comprising $I136^{2.60}$, $W146^{ECL1}$, $P162^{3.29}$, $F224^{4.64}$, $Y352^{7.36}$, and $I355^{7.39}$ (Fig. 3c and Supplementary Fig. 3d). In addition, D18 forms a salt bridge with $R326^{6.55}$, which makes a polar contact with $D351^{7.35}$ and further $S325^{6.54}$, thus constituting an extensive polar interaction network with TM6 and TM7 of ET_AR (Fig. 3d and Supplementary Fig. 3d). These structural observations are supported by the dramatically decreased ET-1 activity on alanine mutants of $K166^{3.33}$, $R326^{6.55}$, and $D351^{7.35}$ (Supplementary Fig. 4a and Table 2). These findings are consistent with a previous report that the C-terminal region is essential for the potency of ET-1[29], of which W21 shows critical roles in receptor binding and activation[30]. Small

molecular antagonists of ET_BR bosentan and K8794 and reverse agonist IRL2500 mimic the hexapeptide of the C-terminal region[21,23], also indicating the importance of this segment in regulating receptor activity. Intriguingly, ET-3 and IRL1620 show an identical C-terminus with ET-1, while s6b and s6c bear a similar hydrophobic replacement from isoleucine to valine at position 19 relative to ET-1 (Fig. 1a). Correspondingly, C-terminus-interacting residues in both ETRs are conserved (Fig. 3e and Supplementary Fig. 5), proposing a conserved receptor-binding mode across these peptides.

The N-terminal region of ET-1 is anchored to the α-helical region by two pairs of intramolecular disulfide bonds. Residues D8-L17 in ET-1 form a helical fold, constituting the architecture of the α-helical region (Fig. 3b). The side chain of D8 forms an H-bond with $Y333^{6.62}$. The phenyl ring of F14 makes hydrophobic interactions with $L344^{7.28}$, $L347^{7.31}$, and $L348^{7.32}$ (Fig. 3f). Residues on ECL2 of ET_AR, including F229, Y231, R232, T238, and M240, are also critical for ET-1 activity through association with the α-helical region of the peptide (Supplementary Fig. 4a and Table 2). The N-terminal region of ET-1 points to the kinked N-terminus of receptor TM5 (Fig. 3b). Compared with the α-helical and C-terminal regions, the N-terminus of ET-1 exposes to the solvent with seldom ET_AR residues making a minimal contribution to ET-1 activity. In contrast to the C-terminus region, the α-helical region, especially the N-terminus of peptide agonists, show lower sequence identity (Fig. 1a), indicating non-conserved binding modes of these two regions and their potential roles in regulating peptide selectivity against ET_AR and ET_BR.

Ligand recognition selectivity for ET_AR and ET_BR

The structures of ET_AR and ET_BR provide templates to explore the mechanism of ligand-binding selectivity. Sequence comparison of ET-1 with two ET_BR selective agonists, ET-3 and IRL1620, reveals that the most noticeable difference resides in the N-terminal region of peptides, in which all replaced amino acids in ET-3 from ET-1 are bulkier (Fig. 1a). This sequence difference elicits a hypothesis that ET_BR has a
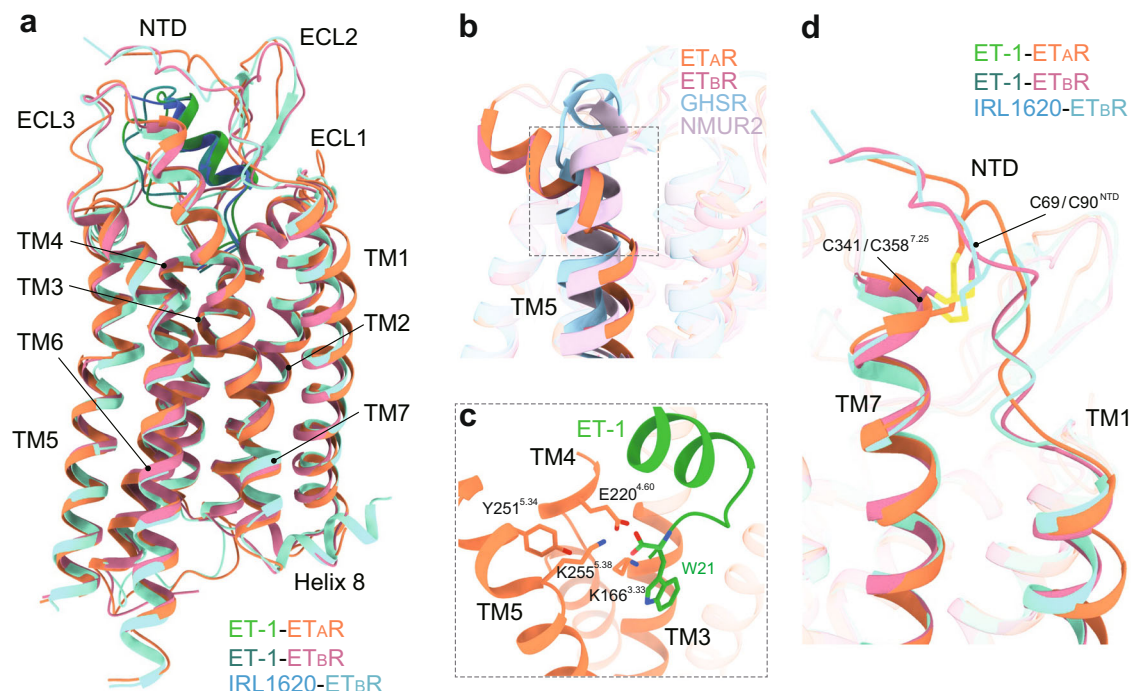
Fig. 2 | Structure features of endothelin receptors in the active state. a Structure superposition of ET1-bound and IRL1620-bound ETRs. **b** Structure superposition of ET-1-bound ETRs and other active class A peptide GPCRs, GHSR (PDB: 7F9Y), and NMUR2 (PDB: 7W55). The notable outward kink of the extracellular part of TM5

upon ETRs activation is highlighted. **c** Polar interaction network that stabilizes the kink conformation of TM5 of ET_AR. **d** The disulfide bond between C69/C90[NTD] and C341/C358[7.25] for ET_AR/ET_BR.
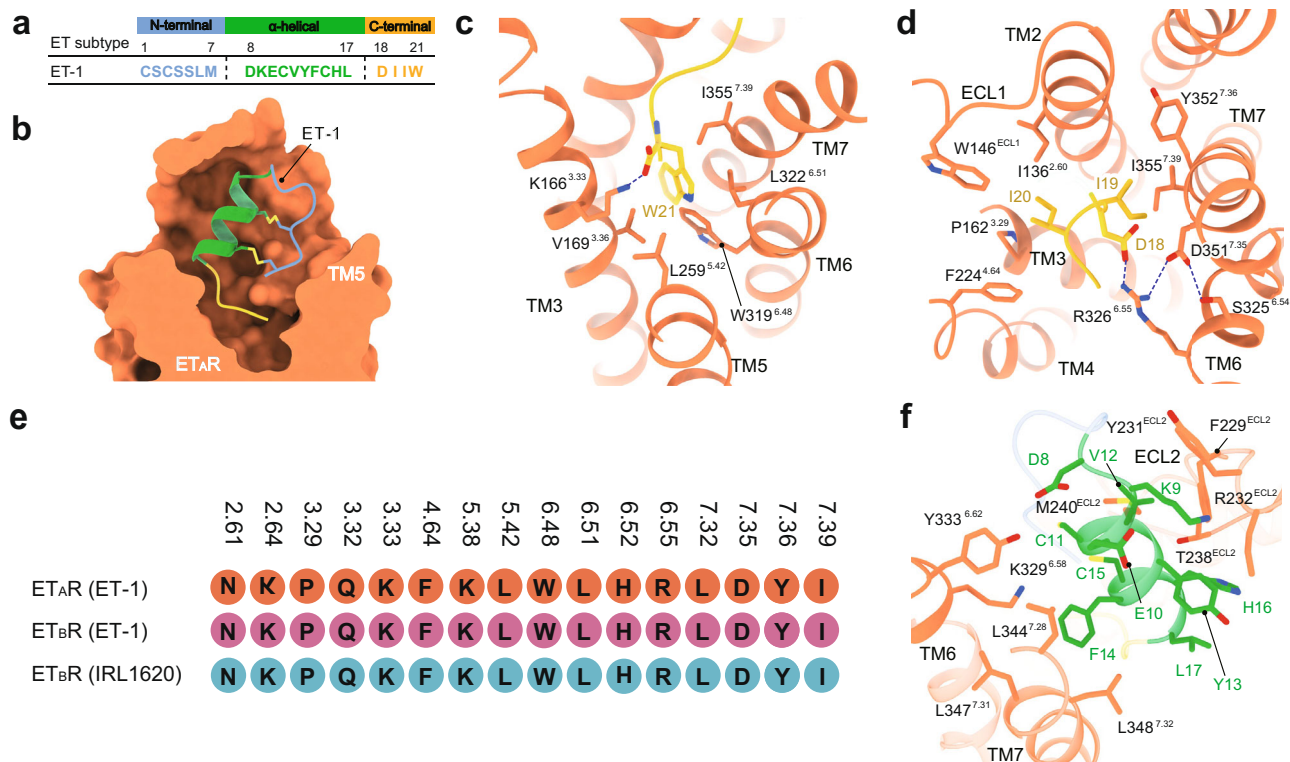
Fig. 3 | Recognition of ET-1 by ET$_A$R. a Sequence of ET-1. The N-terminal, α-helical, and C-terminal regions of ET-1 are colored blue, green, and yellow, respectively. **b** Cross-section of the ET-1-binding pocket in ET$_A$R. Two pairs of intramolecular disulfide bonds of ET-1 are displayed as sticks. ET-1 is shown as a ribbon model with its three regions colored as in **a**. **c**, **d** Detailed interactions between ET-1 and ET$_A$R at the C-terminal region. H-bonds are shown as blue dotted lines. **e** The profile of the interaction residues between the C-terminal region of ligand and endothelin receptors. **f** Detailed interactions between ET-1 and ET$_A$R at the α-helical region.

larger pocket space to accommodate the bulkier N-terminal region of ET-3, which is supported by a smaller pocket size (1976 Å^3, calculated by POVME[31]) for ET$_A$R relative to ET$_B$R (2059 Å^3). This conclusion is in agreement with a previous finding that increasing intramolecular ring size decreased peptide activity at ET$_A$R and shifted the peptide toward ET$_B$R selectivity[32].

Different from ETs, the N-terminal region is absent in agonist IRL1620 (Fig. 1a), which shows over 120,000-fold ET$_B$R selectivity (K_i = 16 pM) over ET$_A$R (K_i = 1900 nM)[15]. Substituting the K9 of ET-1 with the glutamic acid (E9) in IRL1620 increases the electronegativity, which may facilitate the electrostatic interaction with the positively charged extracellular part of ET$_B$R (Fig. 4a, b)[22]. S6c bears an identical substitution from K9 to E9 compared with s6b (Fig. 1a). The charge of the ninth residue has been thought to determine the ETR selectivity of s6c over s6b[33], supporting the importance of electrostatic interaction on peptide selectivity. This theory is also consistent with a previous finding that the net negative electrostatic potential of D8-K9-E10 is essential for ETs binding to ET$_B$R[15]. In addition, the N$^\alpha$-succinylation of IRL1620 and its analogs increased the binding affinity for ET$_B$R, but not ET$_A$R, thus producing ET$_B$R preference[15]. The negative charge of succinylation is more compatible with the positively charged extracellular region of ET$_B$R relative to its cognate receptor, probably contributing to the increased ET$_B$R binding affinity and ET$_B$R selectivity (Fig. 4b).

Activation of endothelin receptors

A structural comparison of ETR-G protein complexes with the crystal structures of ET$_B$R in apo and agonist-, antagonist-, and reverse agonist-bound states reveals that these ETRs are indeed in the active state. TM6 of the ET-1 bound ET$_B$R-G protein complex exhibits a notable outward displacement compared with that of crystal structures of apo (PDB: 5GLI, 4.4 Å, measured at Cα of R318$^{6.30}$), antagonists/inverse agonist bound (PDB: 5XPR and 5×93, 5.4, and 4.6 Å), and the

agonist ET-1 bound ET$_B$R (PDB: 5GLH, 6.8 Å) due to the engagement of G proteins, the hallmark of class A GPCR activation (Fig. 5a). The almost identical active conformation of the ET$_A$R relative to ET$_B$R reveals a conserved activation mechanism in ETRs (Fig. 2a). Thus, structural comparison of the ET-1-ET$_B$R-G$_q$ complex with the apo ET$_B$R was performed to analyze the activation mechanism of ETRs.

On the extracellular side, TM6 and TM7 of ET$_B$R undergo inward movement upon ET-1 binding (3.7 and 4.8 Å, measured at Cα of Y350$^{6.62}$ and R357$^{7.24}$, respectively), compressing the ligand-binding pocket to form compact interactions with the peptide. Meanwhile, the extracellular end of TM2 occurs a lateral shift (2.9 Å, measured at Cα of A164$^{2.67}$), while TM1 shows a smaller extent of inward bend (2.4 Å, measured at Cα of Q91$^{1.22}$) and undergoes a helix-to-loop conformational change (Fig. 5b, c). The potential steric clash between L17 of ET1 and K97$^{1.28}$ of ET$_B$R disturbs the receptor TM1 α-helix from Q91$^{1.22}$ to K97$^{1.28}$ (Fig. 5c). The resulting loop approaches the center of the ligand-binding pocket and forms hydrophobic and van der Waal interactions with the α-helical region of ET-1. In addition, the α-helical region of ET-1 clashes with the N-terminus of ET$_B$R in the apo state, disrupting the latter's interaction with ECL2. Instead, the N-terminus of ET$_B$R covers the ligand-binding pocket and form weak interactions with the N-terminus of the α-helical region of ET-1 (Fig. 5c). These movements of the receptor extracellular ends may propagate to the corresponding cytoplasmic end of the receptor to correspond with the seesaw model of class A GPCR activation, leading to the opening of the cytoplasmic cavity of the helical bundle to accommodate the G protein[34].

Insertion of ET-1 deep into the ligand-binding pocket leads to direct contact of W21 with the toggle switch residue W336$^{6.48}$ in ET$_B$R and triggers their downward movement. Intriguingly, the side chain of I372$^{7.39}$ of ET$_B$R undergoes a downward rotamer shift and a hydrophobic rearrangement with I19 of ET-1, leading to a half-helical downward movement of TM7 (Fig. 5d). In addition, the side chain of
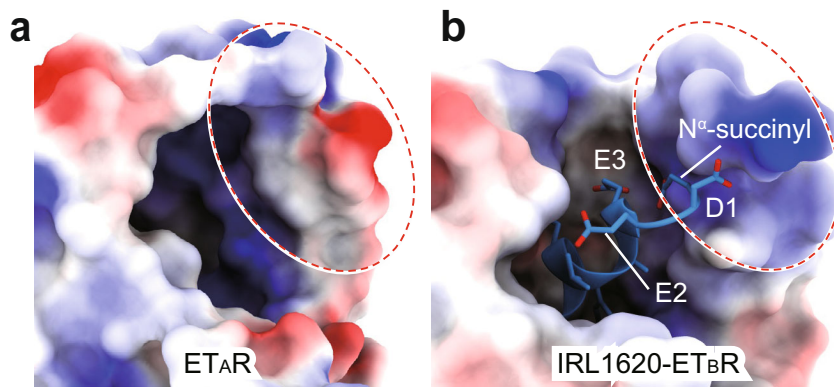
Fig. 4 | Electrostatic surfaces of the ET-1-bound ET_AR and IRL1620-bound ET_BR complex structures. The electrostatic surface presentation of the extracellular regions of ET-1 bound ET_AR (**a**) and IRL1620-bound ET_BR (**b**) are shown. ET-1 in the ET-1-ET_AR complex structure is omitted for a clear presentation. The electrostatic potential was calculated and presented using PyMOL. Deep blue represents positively charged and red represents negatively charged areas.
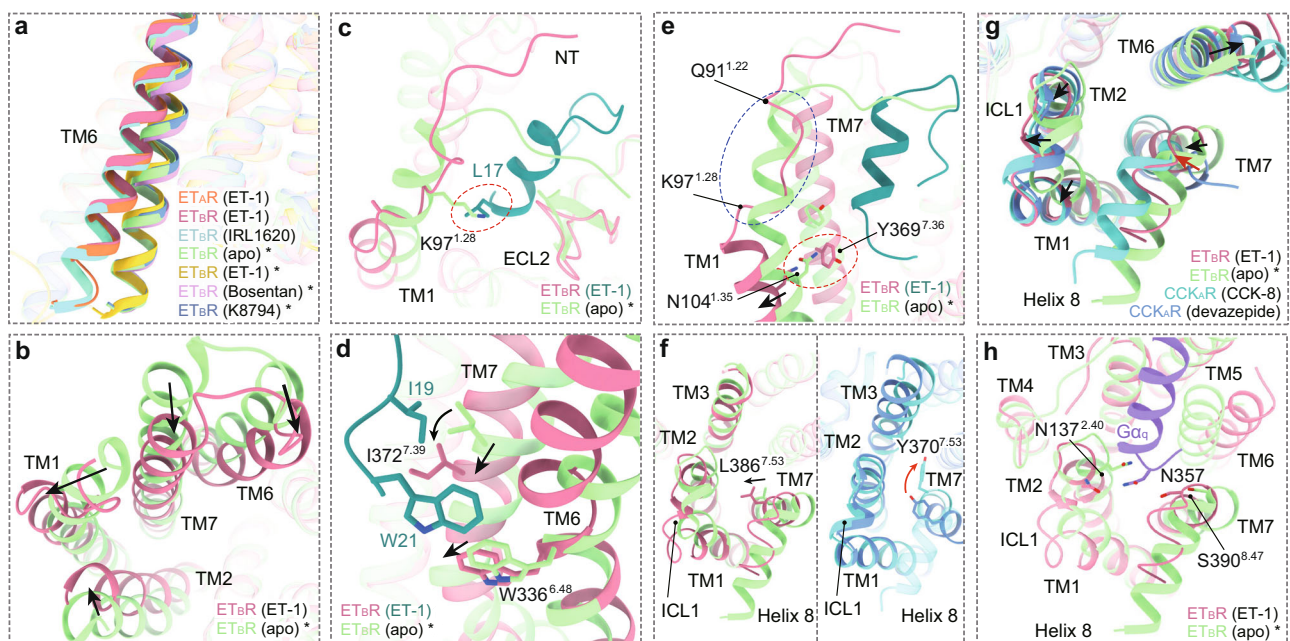
Fig. 5 | Activation and G protein-coupling of endothelin receptors. a Structure superposition of ETR-G protein complexes with the crystal structures of ET_BR in apo (PDB: 5GLI) and agonist- (PDB: 5GLH), antagonist- (PDB: 5XPR), and reverse agonist-bound states (PDB: 5X93). **b** Overall conformational changes of the extracellular side of ET_BR upon ET-1 binding. **c** The potential steric clash between L17 of ET-1 and $K97^{1.28}$ of ET_BR disturbs the receptor TM1 α-helix from $Q91^{1.22}$ to $K97^{1.28}$. The potential clash is highlighted by the red dashed oval. **d** Detailed Interaction between W21, I19 of ET-1 and $W336^{6.48}$, $I372^{7.39}$ of ET_BR. The movement orientations of $W366^{6.48}$, $I372^{7.39}$, and TM7 upon ET_BR activation are indicated as black arrows. **e** Conformation comparison of the extracellular part of TM1 between apo and ET-1 bound ET_BR. The TM1 segment from $Q91^{1.22}$ to $K97^{1.28}$, highlighted in the blue dashed oval, undergoes a helix-to-loop conformational change upon ET_BR activation. The clash between $N104^{1.35}$ and $Y369^{7.36}$ are indicated by a red dashed oval. **f** Differences between the conformational changes of $N^{7.49}P^{7.50}xxY^{7.53}$ motif in ET_BR and CCK_AR. $Y^{7.53}$ in the NPxxY motif is replaced by $L^{7.53}$ in ETRs. The movement of $L386^{7.53}$ in ET_BR and $Y370^{7.53}$ in CCK_AR are indicated by black and red arrows, respectively. **g** Structure superposition of ET-1-bound ET_BR, CCK-8-bound CCK_AR (PDB: 7EZM), the crystal structures of ET_BR in apo (PDB: 5GLI), and devazepide-bound CCK_AR states (PDB: 7F8Y) in cytoplasmic view. Black arrows show the movement directions of the cytoplasmic ends of ET_BR helices upon receptor activation, while the red arrow indicates the shift of TM7 upon CCK_AR activation. **h** The polar interaction linking N357 of the $Gα_q$ subunit and $N137^{2.40}$ and $S390^{8.47}$ of ET_BR.

$Y369^{7.36}$ occurs a remarkable rotation, which probably clashes with $N104^{1.35}$ and pushes TM1 apart from the helical core (Fig. 5e).

The agonist binding propagates agonism signaling downward and triggers the rearrangement of conserved motifs, such as toggle switch, $P^{5.50}V^{3.40}F^{6.44}$, and $D^{3.49}R^{3.50}Y^{3.51}$ (Supplementary Fig. 6a–c). Intriguingly, $Y^{7.53}$ in the conserved $N^{7.49}P^{7.50}xxY^{7.53}$ motif is replaced by leucine in ETRs (Supplementary Fig. 6d). In the classic activation mechanism, the side chain of $Y^{7.53}$ occurs a large amplitude of rotation towards TM3, causing the inward movement of TM7 and strengthening its packing with TM3[35]. Differently, upon ET_BR

activation, $L386^{7.53}$ undergoes a lateral movement towards TM1 and TM2 (Fig. 5f), concomitant with the slight outward movement of these helices together with ICL1 (Fig. 5g), reflective of a unique activation mechanism of ETRs. This conformation may be further stabilized by the insertion of the α5 helix of the Gα subunit, in which N359 makes polar interactions with $S390^{8.47}$ in the TM7-helix 8 hinge region and $N137^{2.40}$ (Fig. 5h). Besides the abovementioned movements of helices, the downward propagated agonism signal eventually leads to the pronounced outward displacement of the cytoplasmic end of TM6, the hallmark of class A GPCRs activation, thus opening the

cytoplasmic cavity of the receptor helix bundle to recruit G proteins (Fig. 5g).

Discussion

Even though extensive efforts have been made, we are still far from fully understanding important issues in the regulation of the endothelin system, although several crystal structures of ET_BR in the inactive state have been released. By determining cryo-EM structures of ET_AR and ET_BR in complex with peptide agonists and G proteins, here we provide molecular evidence to deepen our understanding of the rationale for ligand recognition, subtype selectivity, and activation of endothelin receptors. Our structures present several conformation features upon ETR activation, including the helix-to-loop change of the extracellular portion of TM5, upward half-helical, and shift towards TM1-ICL2-TM2 of TM7 due to unique inter-helical interactions (Fig. 2). Our structures also reveal a conserved recognition mechanism of endothelin isopeptides (ET-1/-2/-3) between both endothelin receptor subtypes (Fig. 3c–e). The identical C-terminus of ETs inserts deep into the ligand-binding pocket of ETRs and is critical for the ET-1-induced ETR activation. The extreme C-terminal residue W21 of ETs directly contacts with toggle switch residue $W^{6.48}$ and triggers familial ETR activation (Fig. 3c). We further provide the structural explanations on peptide selectivity for ETRs, including differences between two ETRs in the pocket sizes and electrostatic potential of the receptor extracellular surface (Fig. 4), and also demonstrate the activation features of ETRs (Fig. 5). Thus, our findings offer an opportunity for designing drugs targeting specific ETR subtypes for the treatment of diseases caused by an endothelin system malfunction.

Methods

Cell culture

Spodoptera frugiperda 9 (*Sf9*) insect cells (Expression Systems, #94-001 F) were grown in ESF 921 serum-free medium (Expression Systems) at 27 °C. AD293 cells (Agilent) were cultured in Dulbecco's modified Eagle's medium (DMEM, Thermo Fisher) supplemented with 10% fetal bovine serum (FBS, Thermo Fisher), and maintained in a humidified chamber with 5% CO_2 at 37 °C.

Constructs

The human wild-type (WT) ET_AR and ET_BR gene was codon-optimized for *Sf9* expression and synthesized by Synbio Technologies. To facilitate the expression and purification, human ET_AR (residues 21–406) and human ET_BR (residues 27–424) DNA was cloned into a modified pFastBac vector (Thermo Fisher), which contains an N-terminal FLAG tag (DYKDDDD) followed by an 8 × His-tag before the receptor using homologous recombination (CloneExpress One Step Cloning Kit, Vazyme). The native signal peptide of the receptors was replaced with the prolactin precursor sequence to increase protein expression.

NanoLuc Binary Technology (NanoBiT, Promega) is originally a structurally complementary reporter system to evaluate protein-protein interaction in cells[36]. NanoBiT is composed of a large subunit (LgBiT, 18 kDa) and an 11 amino acid complementary peptide (SmBiT, peptide, VTGYRLFEEIL) with low affinity for LgBiT, both of which are connected to two interacting target proteins of interest, respectively. When the two proteins interact, the two subunits assemble into an active enzyme and generate a bright luminescent signal in the presence of a substrate. To improve the homogeneity and stability of ETR-G protein complexes, we applied the NanoBiT tethering strategy[24] by fusing a LgBiT subunit at the receptor C-terminus. Rat Gβ1 fuses a HiBiT subunit (peptide 86, VSGWRLFKKIS), a homolog peptide of SmBiT with high affinity for LgBiT[36], with a 15-amino acid (15AA) polypeptide linker (GSSGGGGSGGGGSSG) at its C-terminus (Supplementary Fig. 1).

The Gα$_q$ was designed based on a mini-Gα$_s$ skeleton with an N-terminus replaced by Gα$_i$ for the binding of scFv16. Bovine Gα$_i$ were incorporated with two dominant-negative mutations (G203A and

A326S) by site-directed mutagenesis to increase the stability of the Gαβγ complex and decrease the affinity of nucleotide-binding. The engineered Gα$_q$, Gα$_i$, Gβ1-15AA-HiBiT, and bovine Gγ2 were cloned into the pFastBac vector, respectively. scFv16 was cloned into a modified pFastBac vector which contains a GP67 secretion signal peptide at its N-terminus.

Expression and purification of complexes

Baculoviruses were prepared using the Bac-to-Bac Baculovirus Expression System (Thermo Fisher). *Sf9* insect cells were cultured to a density of 3×10^6 cells per mL and co-infected with FLAG-His 8-ET_AR(21–406)/ET_BR(27–424)-LgBiT, engineered Gα$_q$/Gα$_i$, Gβ1-15AA-HiBiT, Gγ2, and scFv16 baculoviruses at a 1:1:1:1:1 ratio. The cells were then harvested by centrifugation 48 h post-infection and stored at −80 °C for future use.

The frozen cells were thawed on ice and resuspended in lysis buffer containing 20 mM HEPES, pH 7.5, 100 mM NaCl, 10% (v/v) glycerol, 10 mM $MgCl_2$, 5 mM $CaCl_2$, and supplemented with EDTA-free protease inhibitor cocktail (TargetMol). For ET-1-ET_AR-G$_q$/ IRL1620-ET_BR-G$_i$ complex, cells were lysed by dounce homogenization and complex formation was initiated with the addition of 25 mU/mL Apyrase (Sigma-Aldrich) and 10 μM ET-1/ IRL1620 (GenScript) for 1.5 h at room temperature (RT). The membrane was then solubilized by adding 0.5% (w/v) lauryl maltose neopentyl glycol (LMNG, Anatrace) and 0.1% (w/v) cholesterol hemisuccinate (CHS, Anatrace) for 2 h at 4 °C. The sample was clarified by centrifugation at 80,000×*g* for 30 min and the supernatant was then incubated with anti-DYKDDDDK Affinity Beads (GenScript) for 3 h at 4 °C. After incubation, the resin was collected by centrifugation (600×*g*, 10 min) and loaded into a gravity flow column, followed by a wash with 20-column volumes of 20 mM HEPES, pH 7.5, 100 mM NaCl, 10% (v/v) glycerol, 5 mM $MgCl_2$, 1 μM ET-1/IRL1620, 0.01% (w/v) LMNG, and 0.002% (w/v) CHS. The protein was finally eluted with ten-column volumes of 20 mM HEPES, pH 7.5, 100 mM NaCl, 10% (v/v) glycerol, 5 mM $MgCl_2$, 1 μM ET-1/IRL1620, 0.01% (w/v) LMNG, and 0.2 mg/mL FLAG peptide. The purified complexes were concentrated using an Amicon Ultra centrifugal filter (molecular weight cut-off of 100 kDa, Millipore) and then subjected to a Superose 6 Increase 10/300 GL column (GE Healthcare) that was pre-equilibrated with buffer containing 20 mM HEPES, pH 7.5, 100 mM NaCl, 2 mM $MgCl_2$, 1 μM ET-1/IRL1620, 0.00075% (w/v) LMNG, 0.00025% (w/v) GDN, and 0.0002% (w/v) CHS. The purification procedure of ET-1-ET_BR-G$_q$ complex was similar to ET_AR, expect the addition of 0.05% (w/v) digitonin, the final size-column equilibrated with 0.05% (w/v) digitonin instead of 0.00075% (w/v) LMNG, 0.00025% (w/v) GDN, and 0.0002% (w/v) CHS. The monomeric fractions of the complex were collected and concentrated for cryo-EM examination.

Cryo-EM grid preparation and data collection

Three microliters of the purified ET-1-ET_AR-G$_q$-scFv16, ET-1-ET_BR-G$_q$-scFv16, and IRL1620-ET_BR-G$_i$-scFv16 complexes at the concentration of about 18, 10, and 20 mg/mL, respectively, were applied onto glow-discharged holey carbon grids (Quantifoil R1.2/1.3). Excess samples were blotted for 3 s with a blot force of 1 and were vitrified by plunging into liquid ethane using a Vitrobot Mark IV (Thermo Fisher Scientific). Frozen grids were transferred to liquid nitrogen and stored for data acquisition. Cryo-EM imaging was performed on a Titan Krios G4 at 300 kV in the Advanced Center for Electron Microscopy at Shanghai Institute of Materia Medica, Chinese Academy of Sciences (Shanghai, China).

A total of 11,657 movies were collected for the ET-1-ET_AR-G$_q$-scFv16 complex using a Gatan K3 detector in super-resolution mode with a pixel size of 0.824 Å using the EPU. Movies were obtained at a dose rate of about 15 electrons per Å^2 per second with a defocus ranging from −0.8 to −1.8 μm. The total exposure time was 2.35 s, and 36 frames were recorded per micrograph.

For ET-1-ET$_B$R-G$_q$-scFv16 and IRL1620-ET$_B$R-G$_i$-scFv16 complexes, A total of 6750 and 4496 movies were collected by a Gatan K3 detector at a pixel size of 1.04 Å using the EPU, respectively. The micrographs were recorded in super-resolution mode at a dose rate of about 15 electrons per Å^2 per second with a defocus ranging from −0.8 to −2 μm. The total exposure time was 3.13 s, and 36 frames were recorded per micrograph.

Cryo-EM data processing

Cryo-EM image stacks were aligned using RELION-4.0-beta[37]. Contrast transfer function (CTF) parameters for each micrograph were estimated by CTFFIND 4.0[38]. The following data processing was performed using RELION-4.0-beta[37].

For the ET-1-ET$_A$R-G$_q$-scFv16 complex, automated particle selection yielded 13,462,594 particle projections. The projections were subjected to reference-free 2D classification to discard poorly defined particles, producing 665,480 particle projections for further processing. This subset of particle projections was subjected to a round of maximum-likelihood-based three-dimensional classification with a pixel size of 0.824 Å. A selected subset containing 510,362 projections was used to obtain the final map using a pixel size of 0.824 Å. Further 3D classification without image alignment using a mask including only the receptor produced one good subset accounting for 510,197 particles, which were subsequently subjected to 3D refinement and Bayesian polishing. The final refinement generated a map with an indicated global resolution of 3.0 Å and was subsequently post-processed by DeepEMhancer.

For the ET-1-ET$_B$R-G$_q$-scFv16 complex, automated particle selection yielded 7,414,897 particle projections. The projections were subjected to reference-free 2D classification to discard poorly defined particles, producing 1,375,681 particle projections for further processing. This subset of particle projections was subjected to a round of maximum-likelihood-based three-dimensional classification with a pixel size of 1.04 Å. A selected subset containing 415,508 projections was used to obtain the final map using a pixel size of 1.04 Å. Further 3D classification focusing on the receptor without alignment using a mask to mask out the detergent and G protein produced one good subset accounting for 373,655 particles, which were subsequently subjected to 3D refinement, CTF refinement, and Bayesian polishing. The final refinement generated a map with an indicated global resolution of 3.5 Å, and was subsequently post-processed by DeepEMhancer.

For the IRL1620-ET$_B$R-G$_i$-scFv16 complex, automated particle selection yielded 4,078,200 particle projections. The projections were subjected to reference-free 2D classification to discard poorly defined particles, producing 967,642 particle projections for further processing. This subset of particle projections was subjected to a round of maximum-likelihood-based three-dimensional classification with a pixel size of 1.04 Å. A selected subset containing 410,751 projections was used to obtain the final map using a pixel size of 1.04 Å. Further 3D classification focusing the alignment on the receptor produced one good subset accounting for 191,493 particles, which were subsequently subjected to 3D refinement, CTF refinement, and Bayesian polishing. The final refinement generated a map with an indicated global resolution of 3.0 Å.

Model building and refinement

The initial templates of ET$_A$R and ET$_B$R were derived from Alphafold2[39]. Models were docked into the EM density map using UCSF Chimera[40]. The initial models were then subjected to iterative rounds of manual adjustment based on the side-chain densities of bulky aromatic amino acids in Coot[41] and automated refinement in Rosetta and PHENIX[42]. The final refinement statistics were validated using the module "comprehensive validation (cryo-EM)" in PHENIX[42]. The final refinement statistics are provided in Supplementary Table 1. All structural figures were prepared using Chimera[40], Chimera X[43], and PyMOL (https://pymol.org/2/).

NanoBiT assay for β-arrestin recruitment

The NanoBiT assay was used to assess the interaction between ETRs and β-arrestin, which reflects the activity of β-arrestin recruitment by ETRs. Briefly, the full-length ET$_A$R/ET$_B$R and mutants were cloned into the pBiT1.1 vector (Thermo Fisher) with a FLAG tag at its N-terminus and the LgBiT at its C-terminus. Human β-arrestin 2 (residues 1-393, with I386A, V387A, and F388A mutations) was cloned into a pBiT2.1 vector (Thermo Fisher) with the SmBiT at its N-terminus. AD293 cells were cultured in DMEM/high Glucose (GE healthcare) supplemented with 10% (w/v) FBS (Gemini). Cells were maintained at 37 °C in a 5% CO$_2$ incubator with 300,000 cells per well in a six-well plate. Cells were grown overnight and then transfected with 1.5 μg ET$_A$R/ET$_B$R and 1.5 μg β-arrestin constructs by FuGENE® HD transfection reagent in each well for 24 h. Cells were harvested and resuspended in Hanks' balanced salt solution buffer (HBSS) at a density of 5×10^5 cells/ml. The cell suspension was seeded in a 384-well plate at a volume of 10 μl per well, followed by 10 μl HBSS, 10 μl HBSS containing different concentrations of ET-1, and another 10 μl the NanoLuc substrate (furimazine, 1:25 dilution, Promega) diluted in the detection buffer. The luminescence signal was measured with an EnVision plate reader at room temperature.

Receptor surface expression

Cell-surface expression levels of WT or mutants ET$_A$R/ET$_B$R were quantified by flow cytometry. AD293 cells were seeded at a density of 1.5×10^5 per well into 12-well culture plates. Cells were grown overnight and then transfected with 1.0 μg ET$_A$R/ET$_B$R construct by FuGENE® HD transfection reagent in each well for 24 h. After 24 h of transfection, cells were washed once with PBS and then detached with 0.2% (w/v) EDTA in PBS. Cells were blocked with PBS containing 5% (w/v) BSA for 15 min at room temperature before incubating with primary anti-Flag antibody (diluted with PBS containing 5% BSA at a ratio of 1:300, Sigma-Aldrich, F3165) for 1 h at room temperature. Cells were then washed three times with PBS containing 1% (w/v) BSA and then incubated with anti-mouse Alexa-488-conjugated secondary antibody (diluted at a ratio of 1:1000, Thermo Fisher, A-11029) at 4 °C in the dark for 1 h. After another three times of washing, cells were collected, and fluorescence intensity was quantified in a BD Accuri C6 flow cytometer system (BD Biosciences) through a BD Accuri C6 software1.0.264.21 at excitation 488 nm and emission 519 nm. Approximately 10,000 cellular events per sample were collected, and data were normalized to the wild-type ET$_A$R/ET$_B$R. Experiments were performed at least three times, and data were presented as means ± SEM.

Statistical analysis

All functional study data were analyzed using Prism 9 (GraphPad) and presented as means ± SEM from at least three independent experiments. Concentration-response curves were evaluated with a three-parameter logistic equation. EC_{50} is calculated with the Sigmoid three-parameter equation.

Reporting summary

Further information on research design is available in the Nature Portfolio Reporting Summary linked to this article.

Data availability

The data that support this study are available from the corresponding authors upon reasonable request. Density maps have been deposited in the Electron Microscopy Data Bank (EMDB) under accession codes EMD-34663 (ET-1-ET$_A$R-G$_q$-scFv16 complex); EMD-34667 (ET-1-ET$_B$R-G$_q$-scFv16 complex); EMD-34619 (IRL1620-ET$_B$R-G$_i$-scFv16 complex). Structure coordinates have been deposited in the Protein Data Bank (PDB) with accession codes 8HCQ (ET-1-ET$_A$R-G$_q$-scFv16 complex); 8HCX (ET-1-ET$_B$R-G$_q$-scFv16 complex); 8HBD (IRL1620-ET$_B$R-G$_i$-scFv16 complex). Previously published structures can be accessed via

accession codes 7EZM; 7F8Y; 7F9Y; 7W55; 5GLI; 5XPR; 5GLH; 5X93. Source data are provided with this paper.

References

1. Arai, H., Hori, S., Aramori, I., Ohkubo, H. & Nakanishi, S. Cloning and expression of a cDNA encoding an endothelin receptor. *Nature* **348**, 730–732 (1990).
2. Sakurai, T. et al. Cloning of a cDNA encoding a non-isopeptide-selective subtype of the endothelin receptor. *Nature* **348**, 732–735 (1990).
3. Davenport, A. P. International Union of Pharmacology. XXIX. Update on endothelin receptor nomenclature. *Pharm. Rev.* **54**, 219–226 (2002).
4. Regard, J. B., Sato, I. T. & Coughlin, S. R. Anatomical profiling of G protein-coupled receptor expression. *Cell* **135**, 561–571 (2008).
5. Schinelli, S. Pharmacology and physiopathology of the brain endothelin system: an overview. *Curr. Med. Chem.* **13**, 627–638 (2006).
6. Yanagisawa, M. et al. A novel potent vasoconstrictor peptide produced by vascular endothelial cells. *Nature* **332**, 411–415 (1988).
7. Inoue, A. et al. The human preproendothelin-1 gene. Complete nucleotide sequence and regulation of expression. *J. Biol. Chem.* **264**, 14954–14959 (1989).
8. Kloog, Y. et al. Sarafotoxin, a novel vasoconstrictor peptide: phosphoinositide hydrolysis in rat heart and brain. *Science* **242**, 268–270 (1988).
9. Davenport, A. P. et al. Endothelin. *Pharm. Rev.* **68**, 357–418 (2016).
10. Kedzierski, R. M. & Yanagisawa, M. Endothelin system: the double-edged sword in health and disease. *Annu. Rev. Pharm. Toxicol.* **41**, 851–876 (2001).
11. Izume, T., Miyauchi, H., Shihoya, W. & Nureki, O. Crystal structure of human endothelin ETB receptor in complex with sarafotoxin S6b. *Biochem. Biophys. Res. Commun.* **528**, 383–388 (2020).
12. Pandy-Szekeres, G. et al. GPCRdb in 2018: adding GPCR structure models and ligands. *Nucleic Acids Res.* **46**, D440–D446 (2018).
13. Barton, M. & Yanagisawa, M. Endothelin: 30 years from discovery to therapy. *Hypertension* **74**, 1232–1265 (2019).
14. Rubanyi, G. M. & Polokoff, M. A. Endothelins: molecular biology, biochemistry, pharmacology, physiology, and pathophysiology. *Pharm. Rev.* **46**, 325–415 (1994).
15. Takai, M. et al. A potent and specific agonist, Suc-[Glu9,Ala11,15]-endothelin-1(8-21), IRL 1620, for the ETB receptor. *Biochem. Biophys. Res. Commun.* **184**, 953–959 (1992).
16. Maguire, J. J. & Davenport, A. P. Endothelin@25 - new agonists, antagonists, inhibitors and emerging research frontiers: IUPHAR review 12. *Br. J. Pharm.* **171**, 5555–5572 (2014).
17. Huggins, J. P., Pelton, J. T. & Miller, R. C. The structure and specificity of endothelin receptors: their importance in physiology and medicine. *Pharm. Ther.* **59**, 55–123 (1993).
18. Janes, R. W., Peapus, D. H. & Wallace, B. A. The crystal structure of human endothelin. *Nat. Struct. Biol.* **1**, 311–319 (1994).
19. Orry, A. J. & Wallace, B. A. Modeling and docking the endothelin G-protein-coupled receptor. *Biophys. J.* **79**, 3083–3094 (2000).
20. Shihoya, W. et al. Activation mechanism of endothelin ETB receptor by endothelin-1. *Nature* **537**, 363–368 (2016).
21. Shihoya, W. et al. X-ray structures of endothelin ETB receptor bound to clinical antagonist bosentan and its analog. *Nat. Struct. Mol. Biol.* **24**, 758–764 (2017).
22. Shihoya, W. et al. Crystal structures of human ETB receptor provide mechanistic insight into receptor activation and partial activation. *Nat. Commun.* **9**, 4711 (2018).
23. Nagiri, C. et al. Crystal structure of human endothelin ETB receptor in complex with peptide inverse agonist IRL2500. *Commun. Biol.* **2**, 236 (2019).
24. Duan, J. et al. Cryo-EM structure of an activated VIP1 receptor-G protein complex revealed by a NanoBiT tethering strategy. *Nat. Commun.* **11**, 4121 (2020).
25. Kim, K. et al. Structure of a hallucinogen-activated Gq-coupled 5-HT2A serotonin receptor. *Cell* **182**, e1519 (2020).
26. Liu, P. et al. The structural basis of the dominant negative phenotype of the Galphai1beta1gamma2 G203A/A326S heterotrimer. *Acta Pharm. Sin.* **37**, 1259–1272 (2016).
27. Ballesteros, J. A. & Weinstein, H. Integrated methods for the construction of three-dimensional models and computational probing of structure-function relations in G protein-coupled receptors. *Methods Neurosci.* **25**, 63 (1995).
28. Takashima, H. et al. Distributed computing and NMR constraint-based high-resolution structure determination: applied for bioactive Peptide endothelin-1 to determine C-terminal folding. *J. Am. Chem. Soc.* **126**, 4504–4505 (2004).
29. Galantino, M. et al. D-amino acid scan of endothelin: importance of amino acids adjacent to cysteinyl residues in isomeric selectivity. *Pept. Res.* **8**, 154–159 (1995).
30. Tam, J. P. et al. Alanine scan of endothelin: importance of aromatic residues. *Peptides* **15**, 703–708 (1994).
31. Wagner, J. R. et al. POVME 3.0: software for mapping binding pocket flexibility. *J. Chem. Theory Comput.* **13**, 4584–4592 (2017).
32. Wolf, P. & Beck-Sickinger, A. G. The ring size of monocyclic ET-1 controls selectivity and signaling efficiency at both endothelin receptor subtypes. *J. Pept. Sci.* **27**, e3325 (2021).
33. Takayanagi, R. et al. Presence of non-selective type of endothelin receptor on vascular endothelium and its linkage to vasodilation. *FEBS Lett.* **282**, 103–106 (1991).
34. Yin, W. et al. Crystal structure of the human 5-HT1B serotonin receptor bound to an inverse agonist. *Cell Disco.* **4**, 12 (2018).
35. Zhou, Q. et al. Common activation mechanism of class A GPCRs. *Elife* https://doi.org/10.7554/eLife.50279 (2019).
36. Dixon, A. S. et al. NanoLuc complementation reporter optimized for accurate measurement of protein interactions in cells. *ACS Chem. Biol.* **11**, 400–408 (2016).
37. Scheres, S. H. RELION: implementation of a Bayesian approach to cryo-EM structure determination. *J. Struct. Biol.* **180**, 519–530 (2012).
38. Rohou, A. & Grigorieff, N. CTFFIND4: fast and accurate defocus estimation from electron micrographs. *J. Struct. Biol.* **192**, 216–221 (2015).
39. Jumper, J. et al. Highly accurate protein structure prediction with AlphaFold. *Nature* **596**, 583–589 (2021).
40. Pettersen, E. F. et al. UCSF Chimera–a visualization system for exploratory research and analysis. *J. Comput. Chem.* **25**, 1605–1612 (2004).
41. Emsley, P., Lohkamp, B., Scott, W. G. & Cowtan, K. Features and development of Coot. *Acta Crystallogr. D. Biol. Crystallogr.* **66**, 486–501 (2010).
42. Liebschner, D. et al. Macromolecular structure determination using X-rays, neutrons and electrons: recent developments in Phenix. *Acta Crystallogr. D. Struct. Biol.* **75**, 861–877 (2019).
43. Pettersen, E. F. et al. UCSF ChimeraX: Structure visualization for researchers, educators, and developers. *Protein Sci.* https://doi.org/10.1002/pro.3943 (2020).

Author contributions

Y.-J.J. designed the expression constructs, purified the ETR proteins, prepared the final samples for negative stain and cryo-EM data collection, conducted functional studies, and participated in figure and manuscript preparation with the help of J.D.; Q.Y. performed cryo-EM data calculations, model building, and participated in supplementary figure preparation; G.Y., S.Z., and T.G. participated in protein expression and functional studies; X.H. participated in figure preparation; H.J. and X.C. supervised X.H. in figure preparation; K.W. and W.H. participated in cryo-EM grid preparation and data collection; Y.J. and H.E.X. conceived and supervised the project, analyzed the structures, and wrote the manuscript with inputs from all authors.

Competing interests

The authors declare no competing interests.

Additional information

Supplementary information The online version contains supplementary material available at https://doi.org/10.1038/s41467-023-36998-9.

Correspondence and requests for materials should be addressed to Jia Duan, H. Eric Xu or Yi Jiang.

Peer review information *Nature Communications* thanks Jennifer Cash and the other, anonymous, reviewer(s) for their contribution to the peer review of this work.

Reprints and permissions information is available at http://www.nature.com/reprints

Publisher's note Springer Nature remains neutral with regard to jurisdictional claims in published maps and institutional affiliations.